Deterministic incident-wave elevation prediction in intermediate water depth

Umesh A. Korde, Ryan G. Coe & Giorgio Bacelli

Journal of Ocean Engineering and Marine Energy

ISSN 2198-6444

J. Ocean Eng. Mar. Energy
DOI 10.1007/s40722-020-00177-5

ONLINE FIRST

Springer

Journal of Ocean Engineering and Marine Energy
https://doi.org/10.1007/s40722-020-00177-5

RESEARCH ARTICLE

Deterministic incident-wave elevation prediction in intermediate water depth

Umesh A. Korde[1] · Ryan G. Coe[2] · Giorgio Bacelli[2]

Received: 16 February 2020 / Accepted: 2 October 2020

Abstract

Potential performance gains from optimal (non-causal) impedance-matching control of wave energy devices in irregular ocean waves are dependent on deterministic wave elevation prediction techniques that work well in practical applications. Although a number of devices are designed for operation in intermediate water depths, little work has been reported on deterministic wave prediction in such depths. Investigated in this paper is a deterministic wave-prediction technique based on an approximate propagation model that leads to an analytical formulation, which may be convenient to implement in practice. To improve accuracy, an approach to combine predictions based on multiple up-wave measurement points is evaluated. The overall method is tested using experimental time-series measurements recorded in the U.S. Navy MASK basin in Carderock, MD, USA. For comparison, an alternative prediction approach based on Fourier coefficients is also tested with the same data. Comparison of prediction approaches with direct measurements suggest room for improvement. Possible sources of error including tank reflections are estimated, and potential mitigation approaches are discussed.

Keywords Wave prediction · Deterministic · Intermediate water depth · Wave tank experiments · Wave energy devices

List of symbols

$\boldsymbol{\eta}$	Vector of wave elevation measurements at M time instants.
Δh_{lp}	Small change/error in h_{lp}.
ΔT_p	Propagation time error due to propagation model approximation.
Δx_p	Small error in propagation distance due to propagation model approximation.
ℓ	Separation along wave direction between the two wave gauges
$\eta(x; i\omega)$	Wave elevation at point x in the frequency domain (includes amplitude and phase information).
η_1	Wave profile time-series recorded by wave gauge 1
η_2	Wave profile time-series recorded by wave gauge 2
η_{appr}	Wave elevation approximated using Fourier coefficients.
Γ_i	Complex amplitude representing the incident-wave field
Γ_r	Complex amplitude representing the reflected wave field
ω	Angular wave frequency.
ω_n	nth frequency in the Fourier series approximation for the wave elevation at the point of wave measurement.
ω_{mn}	Minimum angular frequency in a realistic spectrum
ω_{mx}	Maximum angular frequency in a realistic spectrum
Ψ	The performance index as defined here for the dispersion relation approximation.
C_n	Amplitude of the nth frequency component in the Fourier series approximation at the point of wave measurement.
θ_p	Phase error due to propagation model approximation.
$A_1, A_2, \ldots, N$	Approximate dispersion relation parameters to be estimated with changing sea states.

✉ Umesh A. Korde
ukorde1@jhu.edu

1 Department of Environmental Health and Engineering, Johns Hopkins University, Baltimore, MD 21118, USA

2 Water Power Technologies (Org. 8822), Sandia National Laboratories, Albuquerque, NM 87185, USA

Published online: 06 November 2020

A_n and B_n	Fourier coefficients estimated using time-series at the point of wave measurement.
A_{nl}, B_{nl}	Fourier coefficients estimated at each measurement location l.
C_n	Amplitude of the nth frequency component in the Fourier series approximation at the point of wave measurement.
d	Distance over which prediction is needed $(x_B - x_A)$.
d_n	Propagation distance from point x_{An} to x_B.
g	Gravity acceleration.
h	Water depth over which waves propagate.
h_0	Nominal depth at which dispersion relation is approximated.
h_l	Propagation impulse-response function.
h_{ln}	Propagation impulse-response function for prediction from point x_{An} to x_B.
J_M	Performance index for estimation of Fourier coefficients A_n and B_n.
$k(\omega)$	Wave number
k_0, ω_0	Regular-wave number k_0 and angular frequency ω_0
k_n	nth wave number in the Fourier series approximation for the wave elevation at the point of wave measurement.
T	Length of time-series of η needed at x_A to predict at x_B.
t	Time variable
t_F	Time instant into the future at which prediction is needed; determined by device dynamics (20-30s; same as t_p).
t_m	mth time instant within a wave elevation time-series approximated using Fourier coefficients.
t_p	Prediction time into the future.
T_{pmx}, T_{pmn}	Propagation times for the smallest and the largest group velocities, respectively.
t_{pn}	Prediction duration from point x_{An} to x_B.
V_{gappr}	Approximate group velocity from propagation model approximation.
v_{gmn}	Minimum group velocity in a realistic spectrum.
v_{gmx}	Maximum group velocity in a realistic spectrum.
x_B	Point where wave elevation prediction is needed
x_p	Propagation distance between point of wave measurement and the point of wave prediction; equivalent to d_p.
x_{An}	nth point within the space–time diagram for prediction from x_A to x_B in practical spectra.
$\mathbf{A}$	Matrix formed by multiplying the two coefficient matrices $\mathbf{C}$ and $\mathbf{S}$.
$\mathbf{A}_l$	Matrix formed by multiplying the two coefficient matrices $\mathbf{C}_l$ and $\mathbf{S}_l$ at each location l.
$\mathbf{C}$	One of the coefficient matrices formed with cosine and sine functions in estimation of A_n and B_n.
$\mathbf{P}$	Vector of coefficients A_n and B_n.
$\mathbf{P}_l$	Vector of coefficients A_n and B_n at each location l.
$\mathbf{S}$	One of the coefficient matrices formed using cosine and sine functions in estimation of A_n and B_n.
$\boldsymbol{\eta}_l$	Vector of wave elevation measurements at location l.
C, S	Fresnel cosine and sine integrals.

1 Introduction

The quest for efficient energy conversion from ocean waves has continued since the early 70s (e.g., Salter 1974; Evans 1976; Budal and Falnes 1977). If waves were regular and sinusoidal, theoretically, 100% conversion would be possible with beam-sea devices in uni-directional waves, under straightforward frequency-domain impedance-matching control (Evans 1981). Such control would also enable capture width ratios[1] > 1 under oscillation constraints for omni-directional devices (Evans 1981), and for slender head-sea devices (Newman 1979). Assuming small-amplitude waves and small-amplitude displacements, similarly high efficiencies can theoretically be achieved in irregular waves. However, the control force required for impedance matching is non-causal and requires deterministic prediction of the incoming wave elevation time-series (Naito and Nakamura 1985; Falnes 1995).

As interest in cost-effective wave energy conversion continues to grow, it seems increasingly important to pursue ways to maximize energy conversion on a real-time, wave-by-wave basis. The purpose of this paper is to investigate deterministic wave prediction as an approach for deriving the optimal control forces for real-time impedance matching. This approach allows the recent, present, and predicted wave surface elevation information to be used as an input (thus preserving both amplitude and phase information in the incoming wave field) to a linear convolution whose non-causal kernel represents the dynamics of the device primary converter. Alternative approaches include methods in which device motion is used to predict excitation force (e.g., Garcia-Abril et al. 2017). Whereas the advantage of deterministic wave prediction is that it enables a

[1] Capture width ratio is defined as average power captured divided by the average wave power incident on the device diameter/width.

direct approach to wave-by-wave impedance matching for performance close to the hydrodynamic optimum, it comes at the expense of an additional wave measurement system (Korde 2015, 2019). As stated in these works, the prediction time was determined based on the dynamics of the device to be controlled, in particular, at least equalling the length of the radiation impulse-response function. The control force impulse-response function can be shown to be an anticausal mirror image of the radiation impulse-response function (e.g., Naito and Nakamura 1985), so that prediction is required at least as far ahead into the future as this impulse-response function has memory in the past. It should be added that the exciting force as commonly expressed in terms of the instantaneous incident-wave elevation is non-causal, so that wave prediction is required far enough into the future also to include the length of the non-causal portion of the exciting-force impulse-response function (Korde and Ringwood 2016).

Deterministic wave elevation prediction based on a single-point wave measurement up-wave of the device was attempted in a wave tank by Naito and Nakamura (1985). Falnes derived the impulse-response function for prediction using a single-point measurement Falnes (1995). Belmont et al. (2007) discussed the impulse-response function for prediction using a single-point measurement ('fixed-point approach') and for prediction in an equivalent situation where a snap-shot measurement over an area was used ('fixed-time approach'). The up-wave fixed-point measurement approach was developed further in Korde (2015) to predict wave elevation at the device 30 s into the future for near-optimal constrained control. The fixed-point approach requires wave elevation measurements at an up-wave point far enough forward where a sufficiently long wave-elevation time history (up to the current instant) allows all practical group velocities in the wave field to be represented at the required future time instant at the device. Analogously, prediction at the required time instant at the device requires a snap-shot measurement over an area large enough to represent all of the practical group velocities included in the approaching wave field (Korde et al. 2017). Note that the prediction model was kinematic. Thus, the dynamic interaction between surface wind and waves in the region of or between the measurement and the device was ignored. Since distances on the order of 1 km appear to be within the coherence range of irregular-wave fields, the kinematic model maybe justified for the purpose at hand (Gran 1987; Falnes 1995; Maa 2013). Long-crested waves in deep water were assumed in these works. Prediction of multi-directional waves is discussed in Belmont et al. (2014). It should be noted that reliable prediction in multi-directional waves may require an approach that recognizes the finite time between successive spatial samples, as obtained, for instance, by a rotating radar. In such a case, a mixed space–time approach based on spectral coefficients may be needed (Al-Ani et al. 2019). Furthermore, for multi-directional waves, it may sometimes be helpful to identify a predominant propagation direction and make predictions along that direction (Al-Ani et al. 2019).

Most of the deterministic prediction work cited above assumes deep-water propagation, where it is straightforward to use analytical integration to derive the linear impulse-response function needed to represent wave propagation. More advanced higher order non-linear reconstruction techniques have been reported in the literature (e.g., Qi et al. 2018). The goal here is to use a computationally light technique that is easily implemented and used in real time. The preference is therefore on a largely analytical technique. The present work aims to extend the deep-water approach to intermediate water depths, and further, also to validate the results against wave tank experiments in intermediate water depths. Wave measurements in the U.S. Navy's Carderock MASK model basin as recorded during a test program carried out by the Sandia National Laboratories were used for this purpose. To facilitate analytical integration, an approximate intermediate-depth propagation model was derived. Intuitively, it is not hard to see that errors are to be expected, and furthermore, errors due to such a model will diverge as propagation distance and prediction time increase, particularly in sea states dominated by longer swells. An approach is investigated here to combine multiple-point wave measurements at different distances from the device to mitigate prediction errors due to the model approximation. The recorded time-series and prediction time for each measurement point are different, and in particular, the closer the measurement point to the device, the shorter are the prediction time and propagation distance possible for that measurement.[2] As seen later in this work, the prediction errors with the approximate prediction model grow with prediction time and prediction distance. For this reason, measurement points closer to the device are likely to yield more accurate predictions based on an approximate propagation model. This point is explained further in the space–time diagram of Sect. 4. Being able to 'average in' predictions from multiple measurements obtained at progressively closer locations thus has the effect of improving the accuracy of the prediction at the device at the correct prediction time as required by the dynamics.

An alternative prediction approach where predictions are based on Fourier coefficients estimated using measurements at an up-wave location (Al-Ani et al. 2019) is also attempted for comparison. This approach also loses accuracy with increasing propagation distance. Averaging the predictions

[2] To obtain the predicted wave elevation at the required time instant in the future, a measurement location that is closer to the device needs a shorter time-series starting at a time determined, such that the prediction time from that location leads to a predicted elevation at the correct time instant in the future as required by the device dynamics. This point is explained further in the space–time diagram of Fig. 1.

based on Fourier coefficient estimates closer to the device also enhances the accuracy of the instantaneous predicted elevations at the device.

This work assumes small-amplitude linear waves, linear superposition, and a linear wave propagation model. In terms of its contribution to knowledge, this work describes how an analytical technique may be used to predict wave elevations in intermediate water depths, wherein the wave frequency and wave-number relation precludes straightforward integration (unlike in deep water or in shallow water). Because the method is approximate, a supplementary technique is introduced, for utilizing multiple point measurements (if available) to improve accuracy. The overall approach is evaluated against experimental tests in a large wave tank, and an approach based on Fourier coefficients that has been reported in the literature. The principal contributions of this work are as follows:

1. an analytical technique to predict in intermediate water depths wave elevation time-series by convolving measured up-wave time-series with an impulse-response function based on an approximation of the intermediate-depth dispersion relation. The approximation is optimized for a chosen kh range, where k denotes wave number and h denotes the water depth.
2. a technique to integrate multiple measurement sets at different points along the propagation direction to improve overall accuracy of prediction based on the approximation above.
3. wave tank tests to investigate accuracy of the technique in a controlled laboratory setting.
4. comparison of the approximated impulse-response-based prediction technique with a method more commonly used by other authors (e.g., Al-Ani et al. 2019).

Whereas the focus of this work is on prediction for use in near-optimal wave-by-wave impedance matching of wave energy devices, In addition, the technique evaluated here should be applicable in control techniques based on model predictive control (Cretel et al. 2011), as well as in ship-motion prediction for on-board and vessel-to-vessel or vessel-to-helicopter operations (Dannenberg et al. 2010). Note that the goal here is to use a physics-based prediction technique to enable non-causal optimal control of floating oscillators. As such, the performance resulting from this approach would serve as a benchmark for other control techniques based on exciting-force measurement and autoregressive prediction (e.g., Liao et al. 2020), while also providing a possible alternative for workers seeking greater performance in energy-poor wave climates or researchers working with exacting requirements for on-board motion control and vessel-to-vessel transfer of sensitive objects/materials.

Section 2 following this introduction reviews propagation model-based prediction in deep water. Section 3 outlines the approximate propagation model that allows analytical integration. Section 4 describes the manner in which predictions from multiple points are combined. Section 5 summarizes the prediction based on Fourier coefficient estimation as applied in this work (see Al-Ani et al. (2019)). Section 5.1 outlines how Fourier coefficients estimated from measurements at multiple points were used here to obtain predictions at the required time instant at the device. The experimental work is summarized in Sect. 6. An uncertainty analysis for the approach based on the approximate propagation model is provided in Sect. 8.1, while the uncertainty associated with the Fourier coefficient-based approach is discussed in 8.2. Results of this work are summarized in Sect. 9, while these results are discussed in Sect. 10.

2 Wave prediction in deep water

Surface gravity waves have a finite coherence time and distance (Gran 1987; Falnes 1995; Maa 2013), and for realistic wind seas and swells, a deterministic propagation model may be appropriate for prediction over a distances ~ 1000 m. Unidirectional or long-crested waves are assumed below, but the approach below should also be applicable to directional wave spectra along a predominant wave direction (e.g., see Al-Ani et al. 2019). For the surface elevation $\eta(x;t)$ at a point x to be Fourier transformable, it is assumed that:

$$\lim_{t\to\pm\infty} \eta(x;t) = 0; \quad \lim_{\omega\to\pm\infty} \eta(x;i\omega) = 0. \tag{1}$$

This assumption restricts prediction to time periods between calm periods with negligible wave activity, and to practical gravity-wave sea states in which wave amplitudes approach zero as frequency approaches infinity. With the further assumption of negligible wind forcing over such distances and prediction times ≤ 30 s, the propagation process for small-amplitude linear waves has been described, in the frequency domain, Naito and Nakamura (1985) and Falnes (1995) as:

$$\eta(x_B;i\omega) = \eta(x_A;i\omega)\mathrm{e}^{-ik(\omega)d}; \quad d = x_B - x_A. \tag{2}$$

Here, d is the propagation distance between the measurement point (for a fixed-point prediction process Belmont et al. (2006)) and the point where prediction is needed (typically, the centroid of the wave energy device). $k(\omega)$ is the wave number, related to the wave angular frequency by the dispersion relation. In deep water, the dispersion relation is approximated as:

$$k(\omega) = \frac{\omega^2}{g}. \tag{3}$$

k has the same sign as ω, for rightward propagation. As stated, it is assumed that $\eta(x;t) \to 0$, as $t \to 0$, and $\eta(x;t) \to 0$ as $t \to \infty$, and further, that $\eta(x;i\omega) \to 0$, as $\omega \to 0$, and as $\omega \to \infty$. The time-domain assumption anticipates that prediction is only attempted between two relatively calm periods. The frequency-domain assumption rests on the observation that realistic surface-wave spectra exclude zero and infinite-frequency oscillations of the water surface. The propagation model in the time-domain can then be described, via inverse Fourier transformation, as an impulse-response function $h_l(t)$, where:

$$h_l(t) = \frac{1}{2\pi} \int_{-\infty}^{\infty} \mathrm{e}^{-k(\omega)d} \mathrm{e}^{i\omega t} d\omega. \tag{4}$$

The dispersion relation form in Eq. (3) is convenient in that it allows $h_l(t)$ to be evaluated analytically as [Falnes (1995), Belmont et al. (2006), Korde (2015)]:

$$\begin{aligned} h_l(t) = & \frac{1}{4}\sqrt{\frac{2g}{\pi d}} \left[\cos\left(\frac{gt^2}{4d}\right) + \sin\left(\frac{gt^2}{4d}\right)\right] \\ & + \frac{1}{2}\sqrt{\frac{2g}{\pi d}} \left[\cos\left(\frac{gt^2}{4d}\right) \mathrm{C}\left(t\sqrt{\frac{g}{2\pi d}}\right)\right. \\ & \left. + \sin\left(\frac{gt^2}{4d}\right) \mathrm{S}\left(t\sqrt{\frac{g}{2\pi d}}\right)\right]. \end{aligned} \tag{5}$$

Here, C and S are the Fresnel cosine and sine integrals, respectively. The prediction distance d and prediction time t_p are related to the group velocity range in the approaching wave fields. The predicted wave elevation can be written as:

$$\eta(x_B; t + t_p) = \int_0^T h_l(\tau)\eta(x_A; t - \tau)\mathrm{d}\tau, \tag{6}$$

where:

$$\begin{aligned} x_B - x_A = d = v_{gmx} t_p; \quad v_{gmx} = \frac{g}{2\omega_{mn}}, \\ T = \frac{d}{v_{gmn}} - \frac{d}{v_{gmx}}; \quad v_{gmn} = \frac{g}{2\omega_{mx}}. \end{aligned} \tag{7}$$

T is the length of the time-series $\eta(x_A; t)$ that needs to be used to include the entire range of group velocities involved in the propagation. Consistent with the assumption that realistic wave spectra do not include zero and infinite-frequency contributions, the maximum group velocity is finite and the minimum group velocity is nonzero, as shown in Fig. 1.

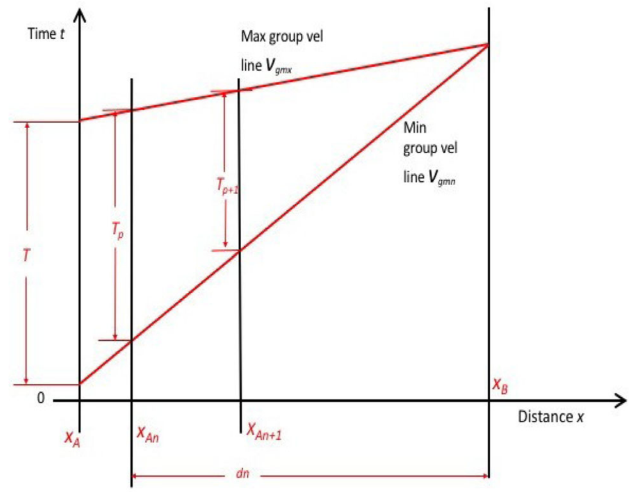

Fig. 1 Space–time diagram for deterministic prediction in practical sea states. Prediction at point x_B at a time instant t_p into the future (i.e., at $t + t_p$) is based on an advancing time-series of length T over $[t - T, t]$, where t denotes the present instant. Prediction over shorter time intervals t_{pn} at x_B is possible from points x_{An} between x_B and x_A using advancing time-series of length T_p up to the current instant.

Results with computer-generated irregular-wave elevations showed agreement within $\pm 7\%$, as discussed in Korde (2015), while unpublished results in narrow-tank tests showed reasonable agreement for short prediction times (Korde and Richon 2018).

3 Propagation in intermediate depths

Prediction for energy-rich swell-dominated sea states in shallow water may be expected to be accurate where propagation is largely non-dispersive, and h_l can again easily be approximated analytically [(Falnes 1995)]. The process is less straightforward for intermediate depths, where the full dispersion relation should be used to describe the propagation kinematics. Thus, at a water depth h:

$$\omega^2 = gk \tanh kh. \tag{8}$$

Given the difficulty of expressing k as an explicit function of ω, analytical evaluation of h_l in Eq. (5) is not straightforward. Analytical evaluation at this stage is preferred, because the entire frequency range $[0, \infty)$ is included in it without discretization. An attempt is made below to derive an analytical approximation to Eq. (8) that could be adjusted to match the dominant periods in incoming sea states. This approach was first discussed in Korde et al. (2019). Rewriting Eq. (8) as:

$$\frac{\omega^2}{g} = k \tanh kh, \tag{9}$$

and approximating the function $\tanh kh$ via a Taylor series expansion around a nominal wave number k_0 (i.e., the dominant wave number for an approaching sea state) and a nominal depth h_0 as:

$$\tanh kh \approx \tanh k_0 h_0 + (kh - k_0 h_0)\mathrm{sech}^2 k_0 h_0 + \cdots . \quad (10)$$

This enables an approximation of Eq. (8) as:

$$\omega^2 \approx gk \tanh k_0 h_0 + gk(kh - k_0 h_0)\,\mathrm{sech}^2 k_0 h_0 + \cdots . \quad (11)$$

The right side can be simplified to a summation where the first term includes both the tanh and sech functions evaluated at kh_0, but is proportional to k; while the second is proportional to k^2. The depth h over the propagation area may not be uniform. In addition, it is expected that new estimations will be made as spectral content changes. Hence, a more general approximation that is patterned after the expression in Eq. (11), but provides more flexibility may be appropriate. Thus, let:

$$\omega^2 \approx A_1 k + A_2 k^2 + \cdots . \quad (12)$$

Here, A_1, A_2, etc. are parameters to be estimated as sea states change. These parameters are estimated to minimize the error between the exact dispersion relation and the approximation. In particular, a functional Ψ is set up, where, e,g., for 2 parameters A_1 and A_2:

$$\Psi = \int_0^\infty \mathcal{L}(A_1, A_2) dk,$$
$$\mathcal{L}(A_1, A_2) \equiv \left[gk \tanh kh - \left(A_1 k + A_2 k^2\right)\right]^2 . \quad (13)$$

For quicker progress, two further approximations are introduced: (i) the integral in Eq. (13) is approximated as a summation over N discrete wave numbers, and (ii) only one parameter, $A_1 \equiv A$ is used. This approximation is expected to work best over a small region of the wave-number space around a predominant wave number in an approaching sea state. The simplification resulting from needing to estimate a single parameter A allows for frequent updates as the spectral content changes over a 10–20-min time span. Thus:

$$\Psi \approx \sum_0^N \left[gk_n \tanh k_n h - Ak_n\right]^2 ; \quad (14)$$

the necessary condition for Ψ to be minimum is:

$$\frac{\partial \Psi}{\partial A} = \sum_0^N \frac{\partial}{\partial A} \left[gk_n \tanh k_n h - Ak_n\right]^2 = 0. \quad (15)$$

This leads to the result:

$$A = \frac{\sum_0^N gk_n \tanh k_n h}{\sum_0^N k_n}. \quad (16)$$

The single parameter A allows the dispersion relation to be expressed as, $\omega^2 = Ak$, which is of the same form as $\omega^2 = gk$, though A is estimated to approximate the intermediate-depth dispersion relation over a small wave-number range. This approximation is convenient in that it enables an analytical approximation of the propagation impulse-response function h_l simply by replacing g in Eq. (5) with A. A needs to be re-estimated when the expected spectral frequency content changes. For each frequency range, however:

$$h_{lA}(t) = \frac{1}{4}\sqrt{\frac{2A}{\pi d}}\left[\cos\left(\frac{At^2}{4d}\right) + \sin\left(\frac{At^2}{4d}\right)\right] + \frac{1}{2}\sqrt{\frac{2A}{\pi d}}\left[\cos\left(\frac{At^2}{4d}\right)\mathrm{C}\left(t\sqrt{\frac{A}{2\pi d}}\right) + \sin\left(\frac{At^2}{4d}\right)\mathrm{S}\left(t\sqrt{\frac{A}{2\pi d}}\right)\right]. \quad (17)$$

The wave elevation at x_B can now be estimated as:

$$\eta(x_B; t + t_p) = \int_0^T h_{lA}(\tau)\eta(x_A; t - \tau)\mathrm{d}\tau. \quad (18)$$

The group velocities in Eq. (7) may be evaluated, for a constant depth h, with the parameter A replacing g.

4 Combining up-wave measurements from multiple points (approximate propagation model)

Non-uniform sea floors can affect prediction accuracy in intermediate waters, particularly when the depth at the point where measurement is made differs from the depth at the device, where prediction is needed. It is proposed that some compensation for model errors due to depth variations may be possible if wave measurements at multiple points up-wave of the device are used in obtaining predictions. It is recalled that the space–time diagram of Fig. 1 explains the relationship between prediction time and time-series length at each measurement point along the propagation direction. Having the measurement points at different distances from the converter buoy would enable averaging over different portions of the space–time diagram in Fig. 1. This is because the prediction times t_p and the input time-series length T need to be adjusted, so that all predictions are made for the same future time instant at the device. The procedure used here is a rudimentary version of a measurement approach based on a phased array of sensors for non-dispersive waves, where sensor-location-dependent delay compensations for each sensor allow all of the 'beams' to be combined in phase at the desired destination point. Such a 'beam-forming' technique is frequently used in microwave and acoustic communications and signal processing (Kumatani et al. 2012). With the x-axis aligned along the dominant wave direction, letting x_{An} be the position of the nth sensor along the predominant direction and x_B be the position of the device, the required wave elevation time-series length and prediction time are determined using:

$$
\begin{aligned}
d_n &= x_B - x_{An},\\
T_n &= \frac{d_n}{v_{gmn}} - \frac{d_n}{v_{gmx}},\\
t_{pn} &= \frac{d_n}{v_{gmx}}.
\end{aligned}
\tag{19}
$$

Because the wave sensors will in general be at different depths, the parameter A_n will be location specific, and the impulse-response function operating on the measurement from the nth sensor would be:

$$
\begin{aligned}
h_{ln}(t) = {} & \frac{1}{4}\sqrt{\frac{2A_n}{\pi d_n}}\left[\cos\left(\frac{A_n t^2}{4d_n}\right) + \sin\left(\frac{A_n t^2}{4d_n}\right)\right]\\
&+ \frac{1}{2}\sqrt{\frac{2A_n}{\pi d_n}}\left[\cos\left(\frac{A_n t^2}{4d_n}\right) \mathrm{C}\left(t\sqrt{\frac{A_n}{2\pi d_n}}\right)\right.\\
&\left. + \sin\left(\frac{A_n t^2}{4d_n}\right) \mathrm{S}\left(t\sqrt{\frac{A_n}{2\pi d_n}}\right)\right].
\end{aligned}
\tag{20}
$$

Each impulse-response function h_{ln} yields a prediction for the surface elevation at the desired time instant (which is determined by the device dynamics). Here:

$$
\eta(x_B; t_F) = \frac{1}{N}\sum_{n=1}^{N} \eta(x_B; t + t_{pn}; x_{An}).
\tag{21}
$$

t_F is the time instant into the future at which prediction is needed as determined by device dynamics (i.e., 20–30 s). t_F has the same meaning as t_p used elsewhere, and is introduced here to avoid confusion. $\eta(x_B; t + t_{pn}); x_{An}$ is derived using:

$$
\eta(x_B; t + t_{pn}; x_{An}) = \int_0^{T_p} h_{ln}(\tau)\eta(x_{An}; t - \tau)\mathrm{d}\tau.
\tag{22}
$$

It should be noted that there is an implicit uniform depth assumption being made at each sensor location in that the depth at that sensor is assumed to be the depth over the propagation region. Given this assumption, for mild variations in the depth, the prediction based on the wave sensor nearest to the device would be most accurate, while the prediction based on the farthest sensor would be least accurate. However, the prediction from the farthest sensor is made necessary by the prediction time requirement, which is determined by the device dynamics. It is proposed here that averaging the predictions of multiple sensors distributed over an area with mildly varying depths will improve the prediction accuracy for the farthest sensor.

Given the approximations embedded in the approach above (specifically, use of the parameter A), it appears worthwhile to compare results with alternative approaches, such as the approach based on Fourier coefficients as employed in recent work (e.g., Al-Ani et al. 2019).

5 Approach based on Fourier coefficients

Thanks to the continued improvements in on-board computer power, methods that rely on Fourier transformations can be used to derive the spectral content of up-wave wave records for prediction into the future at the device location. Similar to the impulse-response based approach of Sect. 3, effects of wind-forcing over the region between the measurement point and the device (where prediction is needed) are ignored. However, errors may arise, particularly close to any spectral peaks, because this technique involves frequency discretization. Additional leakage errors due to the frequency sampling may also occur. Next, because coefficients estimated at one location are to be used to make predictions at another location, the estimation process needs to be designed for predictive quality rather than close match with measured data at any location. It is not clear that the least-squares fitting technique used below (which in essence matches that described in Al-Ani et al. 2019) is optimized for predictive ability, and this aspect may need further attention.

The Fourier coefficients estimation proceeds as follows. A_n and B_n together represent the amplitude and phase of the nth sinusoidal waveform at frequency ω_n. ω_n denotes the nth frequency of a total N frequencies assumed to comprise the irregular-wave time-series sampled. For a wave sensor at x_A, the measured-wave elevation at time $t = t_m$ is:

$$
\begin{aligned}
\eta(x_A; t_m) = \sum_{n=1}^{N} & \left[A_n \cos\left(k_n x_A - \omega_n t_m\right)\right.\\
& \left. + B_n \sin\left(k_n x_A - \omega_n t_m\right)\right].
\end{aligned}
\tag{23}
$$

This expansion assumes that the wave elevation at x_A can be represented as a linear superposition of the wave elevations of N regular waves at N frequencies, each with an amplitude

C_n and phase angle θ_n, where:

$$C_n = \sqrt{A_n^2 + B_n^2}; \quad \text{and} \quad \tan\theta_n = B_n/A_n. \tag{24}$$

A_n and B_n are the Fourier coefficients to be estimated, such that the following 'error' function is minimized at the point x_A where measurement is made. If measurements are made at M time instants, then a 'fitted' surface elevation $\eta_{\text{appr}}(x_A, t_M)$ and the measured-wave elevation $\eta(x_A, t_m)$ can be used, for M time instants, to form a function $J_M(A_n, B_n, n = 1, \ldots, N)$ where:

$$J_M(A_n, B_n, n = 1, \ldots, N) = \sum_{m=1}^{M} \left[\eta(x_A; t_m) - \eta_{appr}(x_A; t_m)\right]^2, \tag{25}$$

with

$$\eta_{\text{appr}}(x_A, t_m) = \sum_{n=1}^{N} [A_n \cos(k_n x_A - \omega_n t_m) + B_n \sin(k_n x_A - \omega_n t_m)]. \tag{26}$$

For the function J_M to be minimum, the following necessary conditions must be satisfied:

$$\frac{\partial J_M}{\partial A_n} = 0; \quad \frac{\partial J_M}{\partial B_n} = 0, n = 1, \ldots, N. \tag{27}$$

Furthermore:

$$\begin{aligned}\frac{\partial J_M}{\partial A_n} &= \sum_{m=1}^{M} \left[\eta(x_A, t_m) - \eta_{appr}(x_A, t_m)\right] \cos(k_n x_A - \omega_n t_m) \\ &= 0,\ n = 1, \ldots, N, \\ \frac{\partial J_M}{\partial B_n} &= \sum_{m=1}^{M} \left[\eta(x_A, t_m) - \eta_{appr}(x_A, t_m)\right] \sin(k_n x_A - \omega_n t_m) \\ &= 0, n = 1, \ldots, N.\end{aligned} \tag{28}$$

The goal of the 'fitting' process is to solve the system of Eq. (28) for A_n and B_n, with $n = 1, \ldots, N$. These equations can be cast in matrix form as follows. Defining a $2N \times M$ matrix $\mathbf{C}$ and an $M \times 2N$ matrix $\mathbf{S}$ as:

$$\mathbf{C} = \begin{bmatrix} c(k_1, t_1) & c(k_1, t_2) & \ldots & c(k_1, t_M) \\ s(k_1, t_1) & s(k_1, t_2) & \ldots & s(k_1, t_M) \\ c(k_2, t_1) & c(k_2, t_2) & \ldots & c(k_2, t_M) \\ s(k_2, t_1) & s(k_2, t_2) & \ldots & s(k_2, t_M) \\ \vdots & \vdots & \ldots & \vdots \\ c(k_N, t_1) & c(k_N, t_2) & \ldots & c(k_N, t_M) \\ s(k_N, t_1) & s(k_N, t_2) & \ldots & s(k_N, t_M) \end{bmatrix}, \tag{29}$$

[where $c(k_n, t_m) = \cos(k_n x_A - \omega_n t_m)$, and $s(k_n, t_m) = \sin(k_n x_A - \omega_n t_m)$]. Furthermore:

$$\mathbf{S} = \begin{bmatrix} c(k_1, t_1) & s(k_1, t_1) & \ldots & c(k_N, t_1) & s(k_N, t_1) \\ c(k_1, t_2) & s(k_1, t_2) & \ldots & c(k_N, t_2) & s(k_N, t_2) \\ \vdots & \vdots & \ldots & \vdots & \vdots \\ c(k_1, t_M) & s(k_1, t_M) & \ldots & c(k_N, t_M) & s(k_N, t_M) \end{bmatrix}. \tag{30}$$

A $2N \times 2N$ matrix $\mathbf{A}$ can be defined, such that:

$$\mathbf{A} = \mathbf{CS}. \tag{31}$$

The $2N \times 1$ vector $\mathbf{P} = [A_1, B_1, \ldots, A_N, B_N]^T$ of parameters can be evaluated as:

$$\mathbf{P} = \mathbf{A}^{-1}\mathbf{C}\boldsymbol{\eta}, \tag{32}$$

where $\boldsymbol{\eta} = [\eta(x_A, t_1), \eta(x_A, t_2), \ldots, \eta(x_A, t_M)]^T$ is the vector of wave elevation measurements. With the coefficients $A_n, B_n, n = 1, \ldots, N$ thus determined, the wave elevation t_p seconds ahead at x_B (where the device is) can be found as:

$$\eta(x_B, t + t_p) = \sum_{n=1}^{N} \left[A_n \cos\left(k_n x_B - \omega_n(t + t_p)\right) + B_n \sin\left(k_n x_B - \omega_n(t + t_p)\right)\right]. \tag{33}$$

5.1 Using measurements at multiple points (Fourier coefficient approach)

When measurements at multiple locations are available, the coefficients estimated for each location can be used to derive the predicted wave profile. Then, if concurrent measurements are available at each l of L measurements points, A_{nl} and B_{nl} can be estimated at each l as:

$$\mathbf{P}_l = \mathbf{A}_l \mathbf{C}_l \boldsymbol{\eta}_l. \tag{34}$$

where:

$$\boldsymbol{\eta}_l = [\eta(x_l, t_1)\ \eta(x_l, t_2)\ \eta(x_l, t_3)\ \ldots \eta(x_l, t_M)]^T. \tag{35}$$

Using $\mathbf{P}_l$, the predicted elevation at time $t + t_p$ may be obtained:

$$\eta(x_B; t + t_p; l) = \sum_{n=1}^{N} \left[A_{nl} \cos\left(k_n x_B - \omega_n(t + t_p)\right) + B_n \sin\left(k_n x_B - \omega_n(t + t_p)\right)\right]. \tag{36}$$

Averaging over L predictions for each time instant,

$$\eta(x_B; t+t_p) = \frac{1}{L}\sum_{l=1}^{L}\eta(x_B; t+t_p; l). \tag{37}$$

6 Experimental work

All testing was carried out in the Maneuvering and Seakeeping basin (MASK) at Carderock Division, Naval Surface Warfare Center located in Bethesda, Maryland. The MASK is an indoor basin with an overall length of 110 m (360 ft), a width of 73 m (240 ft), and a depth of 6.1 m (20 ft) except for a 10.7 m (35 ft) deep trench that is 15.2 m (50 ft) wide and parallel to the long side of the basin. This is located on the south side. The side view and plan view of the tank are shown in Fig. 2 (Brownell 1962).

The MASK wavemaker system consists of 216 paddles. There are 108 paddles along the North edge of the basin ($x = 0$ in Fig. 3), 60 paddles in a ninety degree arc, and 48 paddles along the West edge of the basin ($y = 0$ in Fig. 3). The wavemaker control is driven by force feedback, as designed and installed by Edinburgh Designs, Ltd. Along the two edges of the basin opposite of the wavemakers are artificial beaches with a 12° slope. The beaches are composed of seven concrete layers, and are effective in dissipating energy and mitigating the mass flux of water back into the tank during wave generation. The hydrodynamic properties of the tank were first reported in Brownell (1962).

Figure 3 shows the locations of the wave sensors used in these tests. Wave propagation is at 70° with respect to the north wall (the horizontal axis in Fig. 3. Time-series wave elevation measurements made by the Bridgeprobe wave gages (located along the propagation direction) are used for all comparisons in the present work. More details are included in Coe et al. (2018).

7 Estimating reflections

Since the focus of this work was on verifying the effectiveness of an approximate analytical model for deterministic wave prediction, it was considered important to quantify possible uncertainties in the test data due to any reflections from the beaches. During an early part of the tests, the Bridgeprobe wave gauges were used to make wave profile measurements in regular waves. It should be mentioned that the present tests were performed with a device model in place. However, the model was held fixed during these tests and contributes only a diffracted wave field. For wave frequencies at which $\lambda/D \gg 1$ (λ and D bering the wavelength and model diameter, respectively), diffraction effects are expected to be small, while, for $\lambda/D \leq 1$, reflections from the model may not be negligible and will enter the measured-wave records. It is expected therefore that the results of the present reflection quantification will include model reflections in addition to beach reflections. Methods to identify incident and reflected wave components in uni-directional waves in wave tanks have been of interest for decades. Goda and Suzuki (1976) used a technique to separate incident and reflected wave contributions using two wave gauges placed a known length apart along the propagation direction. A method based on three wave gauges was tested by Mansard and Funke (1980). The method used here was based on the more expedient Goda and Suzuki approach. Given the existence of singularities at certain wavelength–probe separation combinations, the present technique was implemented for regular waves. This is justified for the small-amplitude linear waves assumed throughout this work (for which linear superposition of components at different amplitudes, frequencies, and phases would produce an irregular-wave field). Finally, attenuation/dissipative effects of tank walls and floor are not considered here.

Below, the wave profile measured by wave gauge 1 is denoted as $\eta_1(t)$ and that measured by wave gauge 2 as $\eta_2(t)$. The wave profiles measured by the two probes both contain the incident-wave field approaching the beach and the reflected wave field traveling back to the wavemakers. The location of wave gauge 1 is set as 0, and the location of wave gauge 2 as ℓ, where ℓ is measured along the incident-wave propagation direction. For a given regular-wave combination of wave number k_0 and ω_0, the two wave profiles can be represented as:

$$\eta_1(t) = \Re\left[\Gamma_i e^{i\omega_0 t} + \Gamma_r e^{i(-k_0\ell+\omega_0 t)}\right], \text{ and,}$$
$$\eta_2(t) = \Re\left[\Gamma_i e^{-i(k_0\ell-\omega_0 t)} + \Gamma_r e^{i\omega_0 t}\right]. \tag{38}$$

Here, Γ_i and Γ_r are complex quantities containing both amplitude and phase information. The reflected wave travels in a direction opposite to the incident wave. $\Re$ stands for 'real-part'. Recall that ℓ denotes the distance between the two probes along the wave propagation direction. In Eq. (38), Γ_i and Γ_r denote the incident and reflected wave contributions to η_1 and η_2.

The wave elevation time-series η_1 and η_2 for a regular wave of frequency ω_0 can be expressed as (phases are included in the complex amplitudes):

$$\eta_1(t) = \Re\left[\Gamma_1 e^{i\omega_0 t}\right], \text{ and, } \eta_2(t) = \Re\left[\Gamma_2 e^{i\omega_0 t}\right]. \tag{39}$$

The Fourier transforms of η_1 and η_2 can be expressed as (assuming $\eta_1, \eta_2 \to 0$ as $t \to \pm\infty$):

Fig. 2 Side and top views of the MASK wave basin Brownell (1962).

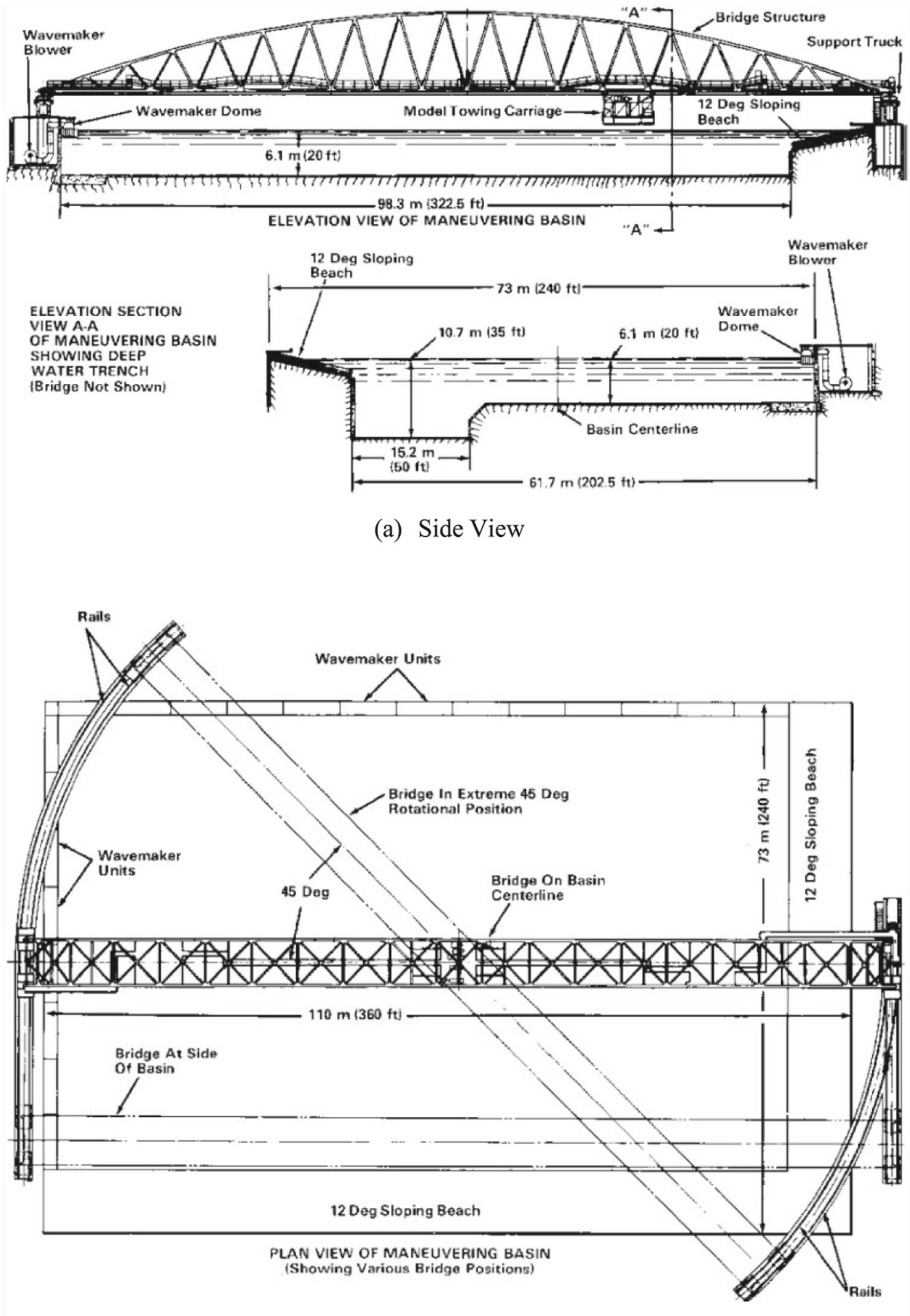

(a) Side View

Plan View

$$\int_{-\infty}^{\infty} \eta_1(t) \mathrm{e}^{-i\omega t} \mathrm{d}\omega, \quad \text{and} \quad \int_{-\infty}^{\infty} \eta_2(t) \mathrm{e}^{-i\omega t} \mathrm{d}\omega. \tag{40}$$

The Fourier transforms of the right sides of Eq. (38) are, respectively:

$$\int_{-\infty}^{\infty} \Gamma_i \mathrm{e}^{i\omega_0 t} \mathrm{e}^{-i\omega t} \mathrm{d}t + \int_{-\infty}^{\infty} \Gamma_r \mathrm{e}^{i(-k\ell+\omega_0 t)} \mathrm{e}^{-i\omega t} \mathrm{d}t,$$
$$\int_{-\infty}^{\infty} \Gamma_i \mathrm{e}^{-i(k_0\ell-\omega_0 t)} z + \int_{-\infty}^{\infty} \Gamma_r \mathrm{e}^{-i\omega_0 t} \mathrm{e}^{-i\omega t} \mathrm{d}t. \tag{41}$$

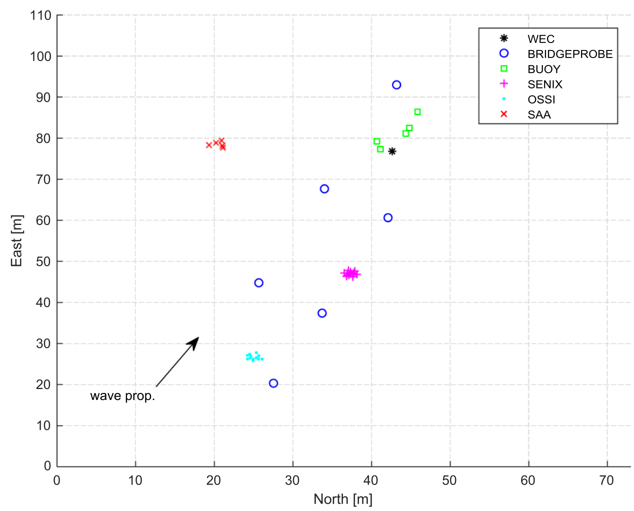

Fig. 3 Wave tank layout showing wave probe locations along the wave propagation direction (Coe et al. 2018).

Evaluating the Fourier transforms in Eq. (40) and using substitutions from Eq. (39):

$$\Gamma_1 \delta(\omega - \omega_0) = \Gamma_i \delta(\omega - \omega_0) + \Gamma_r \mathrm{e}^{-ik\ell} \delta(\omega - \omega_0),$$
$$\Gamma_2 \delta(\omega - \omega_0) = \Gamma_i \mathrm{e}^{-ik\ell} \delta(\omega - \omega_0) + \Gamma_r \delta(\omega - \omega_0). \quad (42)$$

Here, the fact that the delta function is even has been used. In matrix form:

$$\boldsymbol{\Gamma}_m = \mathbf{R} \boldsymbol{\Gamma}_p. \quad (43)$$

Here, $\boldsymbol{\Gamma}_m = [\Gamma_1,\ \Gamma_2]^T$, $_p = [\Gamma_i, \Gamma_r]^T$. The matrix $\mathbf{R}$ is just:

$$\mathbf{R} = \begin{bmatrix} \mathrm{e}^{-ik_0\ell} & 1 \\ 1 & \mathrm{e}^{-ik_0\ell} \end{bmatrix}. \quad (44)$$

When $\mathbf{R}$ is nonsingular, the incident and reflected complex amplitudes can be found by inverting the relation in Eq. (43). Using some algebra, $\mathbf{R}^{-1}$ can be expressed as:

$$\mathbf{R}^{-1} = \frac{1}{2i \sin k\ell} \begin{bmatrix} \mathrm{e}^{ik_0\ell} & -1 \\ 1 & \mathrm{e}^{ik\ell} \end{bmatrix}. \quad (45)$$

The incident and reflected complex amplitudes can now be expressed as:

$$\Gamma_i = \frac{1}{2i \sin k_0\ell} \left[\Gamma_1 \mathrm{e}^{ik_0\ell} - \Gamma_2 \right],$$
$$\Gamma_r = \frac{1}{2i \sin k_0\ell} \left[-\Gamma_1 + \Gamma_2 \mathrm{e}^{ik_0\ell} \right]. \quad (46)$$

$\mathbf{R}$ is singular for $k_0\ell = n\pi$. The singularities may be avoided by altering the spacing ℓ between the wave gauges.

The reflection coefficient R_M can be found using:

$$R_M = \frac{|\Gamma_r|}{|\Gamma_i|}. \quad (47)$$

R_M can be expressed in percentage form. The wave gauges Bridgeprobe 8 and Bridgeprobe 6 were chosen as the two probes designated 1 and 2 in this work. The regular-wave records at the two locations were Fourier transformed in MATLAB to obtain the complex amplitudes Γ_1 and Γ_2. It was ensured that early parts of the records containing transients were removed prior to use. This approach based on direct use of complex amplitudes helps to avoid potentially error-prone phase measurement following Fourier transformation. Such a phase estimation would be required with the Goda and Suzuki technique as proposed. The results obtained here are subject to measurement uncertainties arising from the individual wave probe operation and the repeatability of the overall tank hardware. An uncertainty of $\pm 1\%$ was assumed for this work, based on prior experience with the use of the overall tank hardware.

8 Uncertainty analysis

8.1 Prediction errors with approximate propagation-model approach

The predictions as obtained using the propagation model-based technique are subject to uncertainty due to the imperfections in the model. The principal source of uncertainty is the present approximation to the dispersion relation. Over the propagation distance and prediction time of interest, other sources of uncertainty are, possible non-uniform water depth, sudden changes in sea state and predominant direction, wave–wave non-linear interaction, etc. Depth non-uniformities over the propagation distance and errors due to dispersion relation approximation are expected to be mitigated partially by the use of multiple measurement points distributed over the up-wave wave field.

Because the dispersion relation approximation is essential to the present analytical integration based prediction framework, it is important to estimate its contribution to the uncertainty in the predicted wave elevation time-series. The uncertainty estimate derived below forms the lower bound of the overall uncertainty, as all other sources of uncertainty have been ignored as non-dominant. Uncertainty sources neglected here include small-wave directionality, non-linear interactions, slow changes in sea states, measurement errors, and depth non-uniformities. The predicted wave elevation at x_B using a measured time-series at x_A is as discussed earlier:

$$\eta(x_B; t+t_p) = \int_t^T h_{lp}(\tau)\eta(x_A, t-\tau)\mathrm{d}\tau. \tag{48}$$

Denoting the uncertainty on $\eta(x_B; t+t_p)$ as $\Delta\eta(x_B; t+t_p)$:

$$\Delta\eta(x_B; t+t_p) = \int_t^T \Delta h_{lp}(\tau)\eta(x_A, t-\tau)\mathrm{d}\tau. \tag{49}$$

For uni-directional waves, and for waves that are small enough for wave–wave interactions to be ignored for a given frequency range in a spectrum, the dominant source of error is expected to be the dispersion relation approximation. If the impulse-response function h_{lp} is applied over a propagation distance x_p, then:

$$\begin{aligned} h_{lp}(t) = &\frac{1}{4}\sqrt{\frac{2A}{\pi x_p}}\left[\cos\left(\frac{At^2}{4x_p}\right) + \sin\left(\frac{At^2}{4x_p}\right)\right] \\ &+ \frac{1}{2}\sqrt{\frac{2A}{\pi x_p}}\left[\cos\left(\frac{At^2}{4x_p}\right)\mathrm{C}\left(t\sqrt{\frac{A}{2\pi x_p}}\right)\right. \\ &\left.+ \sin\left(\frac{At^2}{4x_p}\right)\mathrm{S}\left(t\sqrt{\frac{A}{2\pi x_p}}\right)\right]. \end{aligned} \tag{50}$$

As shown in Fig. 1, the propagation distance x_p denotes the distance over which a prediction can be made from a measurement x_{An}, and t_p is the corresponding prediction time. x_{An} denotes one of the intermediate locations between x_A and x_B over which measurements are made. Prediction at distance x_p and time t_{pn} from x_{An} requires a time-series T_p seconds long. With h_{lp} denoting the impulse-response function for prediction from x_{An} over (x_p, t_{pn}):

$$\Delta h_{lp}(t) = \left|\frac{dh_{lp}}{dx_p}\right| \Delta x_p. \tag{51}$$

$\Delta h_{lp}(t)$ is expected to cause both a mismatch in actual elevation magnitude and a time lead/lag. These effects would manifest as amplitude and phase errors in the frequency domain. The propagation distance error Δx_p due to the dispersion relation approximation can be estimated as follows. For a propagation distance x_p, if the propagation time for the slowest waves (highest frequency ω_{mx} with a non-negligible amplitude $A(\omega_{mx})$) is T_{pmx} (longest time). The propagation time for the fastest waves (smallest frequency ω_{mn} with a non-negligible amplitude $A(\omega_{mx})$) is T_{pmn} (shortest time), expressed as:

$$T_{pmx} = \frac{x_p}{v_{gmn}}; \quad T_{pmn} = \frac{x_p}{v_{gmx}}. \tag{52}$$

Here, v_{gmx} and v_{gmn} are the greatest and smallest group velocities represented in an incoming spectrum. With v_g denoting the group velocity at an arbitrary frequency:

$$v_g = \frac{1}{2}\frac{\omega}{k}\left[1 + \frac{2kh}{\sin 2kh}\right]. \tag{53}$$

The underlying dispersion relation is Newman (1978):

$$\omega^2 = gk\tanh kh. \tag{54}$$

With an approximation such as:

$$\omega^2 \approx Ak, \tag{55}$$

$$v_{\text{gappr}} = \frac{d\omega}{dk} = \frac{A}{2\omega}. \tag{56}$$

The propagation distance uncertainty Δx_p over a prescribed time duration T_0 can be estimated as:

$$\Delta x_p = \left(v_g - v_{gappr}\right) T_0 = \frac{1}{2}\left[\frac{\omega}{k}\left(1 + \frac{2kh}{\sin 2kh}\right) - \frac{A}{\omega}\right] T_0. \tag{57}$$

Δx_p at a frequency ω can then be expressed as:

$$\Delta x_p = \frac{T_0}{2\omega}\left[g\left(\tanh kh + \frac{kh}{\cosh^2 kh}\right) - A\right]. \tag{58}$$

The propagation time uncertainty ΔT_p can be estimated as:

$$\Delta T_p = \frac{\Delta x_p}{v_g}. \tag{59}$$

The phase error θ_p at each frequency can be found as:

$$\theta_p = \omega\Delta T_p. \tag{60}$$

8.2 Prediction errors with Fourier coefficient-based prediction

The Fourier coefficient-based approach has been discussed and investigated by detail by Belmont et al. (2014), Al-Ani et al. (2019), etc. Possible errors stemming from this approach include (i) introduction of an additional frequency due to the implicit assumption of periodicity of the time-series used for estimating the coefficients, (2) spectral leakage due to wave periods that cannot fully be accommodated within the sampled length of the time-series, and (3) aliasing, if the sampling frequency is smaller than the highest likely frequency in the sampled time-series. Of these, the aliasing possibility can be avoided with a large enough sampling frequency (here > 50 Hz). Spectral leakage errors can be minimized with the use of zero-filling (Press et al. 1986).

Because Fourier series approximation is integral to this estimation approach, and because the wave elevation time-series is of finite length, there is a frequency $1/T_s$ introduced in the fitted time-series (i.e., the time-series actually represented by the coefficients A_n and B_n). If a long enough time-series measurement is not available for this estimation, this $1/T_s$ frequency is likely to be a low frequency that falls within the frequency range where wave activity does occur, and could cause significant errors.

Errors are also likely in the coefficients A_n and B_n themselves, due to errors in the linear system solution of Eq. (32). As discussed in Al-Ani et al. (2019), these errors are driven by the condition number of the matrix $\mathbf{A}$. A small condition number ≤ 10 is desired. In the present calculations, a condition number $C_n = 3.17$ was observed. For this reason, errors in A_n and B_n due to inaccurate solution of Eq. (32) are not expected to be significant in the present case. In this work, the number N of the coefficients A_n, B_n was chosen to be 512. This was arrived at following a convergence study, starting with $N = 128$ and going up in a sequence to $N = 1024$. At the lower values of N, amplitude errors were found to be considerably greater, steadily falling as N approached 512. The $\mathbf{C}$ matrix became singular for $N = 1024$. Note that N was chosen to be a power of 2 for seamless Fourier transformation and inverse Fourier transformation.

9 Results

Reflection coefficients (as percentages of incident-wave amplitudes) with error bars found using the method of Sect. 7 are shown in Fig. 4. Figures 5 and 6 plot the errors resulting from the present propagation model approximation. Errors with respect to propagation distance and propagation time are both shown. For the distance of $\sim$ 75 m between the wave probes Bridgeprobe 1 and Bridgeprobe 6, a prediction time $t_p = t_F = 9.53$s was used in the test cases. The prediction times t_{pn} between Bridgeprobe 2 and Bridgeprobe 6, and Bridgeprobe 3 Bridgeprobe 6, etc. were shorter and governed by the respective distances between the probes. Figure 7 compares the time-series results for predicted wave elevation based on the approximate propagation model with the measured-wave elevation at the same location. Results were as obtained from wave tank measurements for a representative test run. Figure 8 compares prediction results for the Fourier coefficients based approach with the measured-wave elevation time-series. Figure 9 plots the results obtained by combining predictions from multiple locations using the approximate propagation model. Figure 10 shows the results for predictions based on Fourier coefficients estimated at multiple locations. Results are compared with measurements in both cases. The Fourier transforms of the squares of the instantaneous elevations are compared in Figs. 11 and 12, for

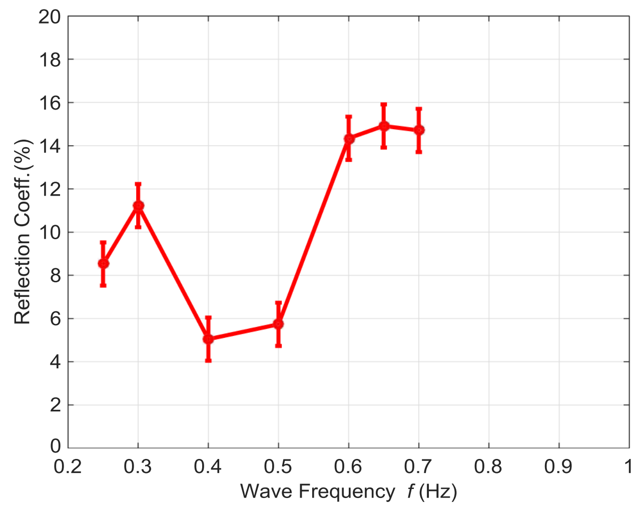

Fig. 4 Percentage ratio of reflected and incident-wave amplitudes as a function of wave frequency in regular waves. Note that these results also include reflections from the device model.

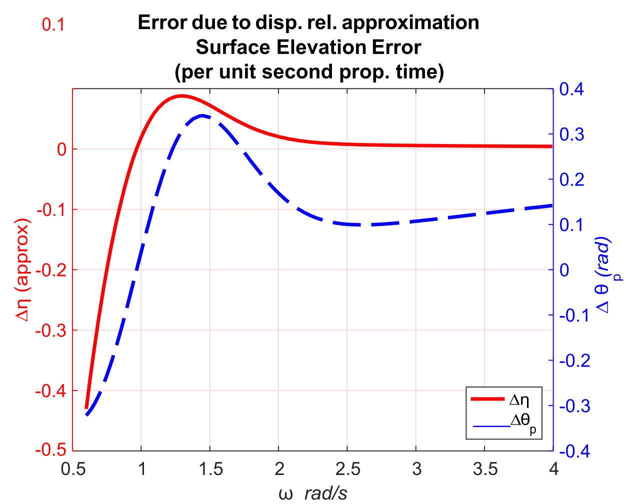

Fig. 5 Errors due to dispersion relation approximation: approximate frequency distribution for errors in wave amplitude when the approximate propagation model is used for wave elevation prediction in intermediate water depth

the results based on 5 point measurements. Because the tank depth over the test section was uniform, the prediction techniques were not impacted by effects of non-uniform depth. Finally, to allow comparison of the two prediction approaches relative to each other, Fig. 13 compares the Fourier transforms of the squares of the instantaneous elevations. Results are discussed in the following section.

10 Discussion of results

It should be noted that the deep-water propagation model was studied and its results were compared with numerically generated deep-water wave time-series in an earlier work

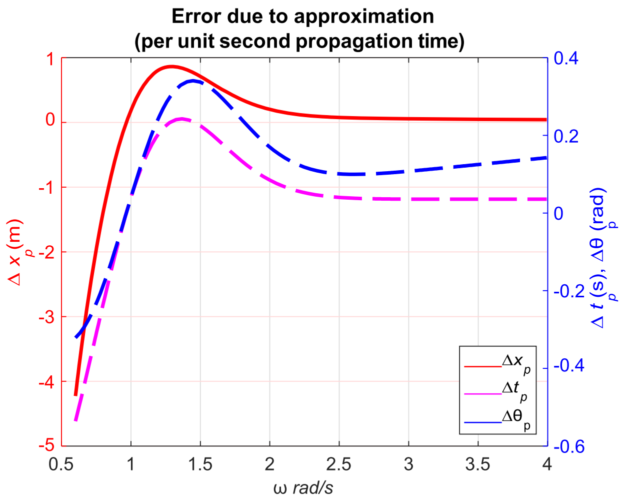

Fig. 6 Errors due to dispersion relation approximation: approximate frequency distribution for errors in wave phase when the approximate propagation model is used for wave elevation prediction in intermediate water depth.

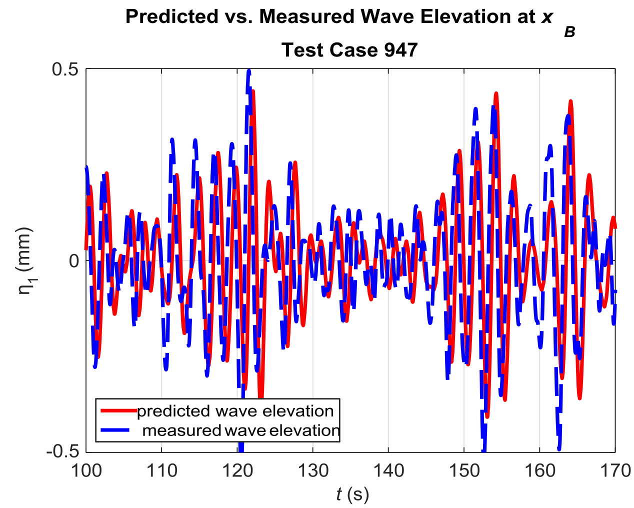

Fig. 7 Predicted vs. measured-wave elevation (proposed approximation): wave elevation time-series as predicted using the approximate intermediate-depth propagation model. Experimental measurements for the prediction location are also shown.

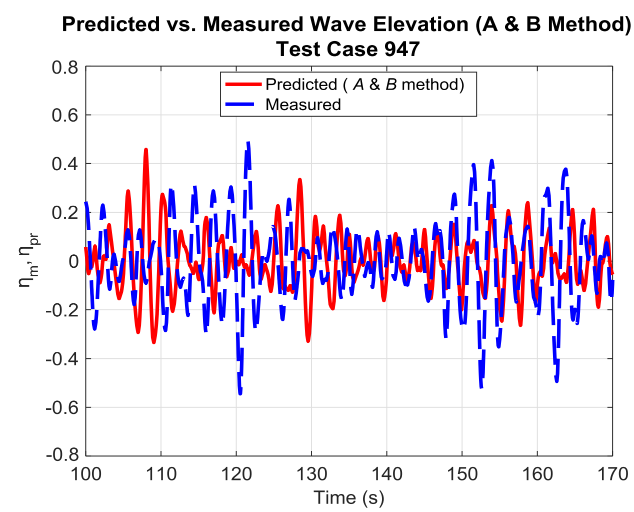

Fig. 8 Predicted vs. measured-wave elevation (Fourier coefficients): wave elevation time-series as predicted using the method based on Fourier coefficients (A and B method). Experimental measurements for the prediction location are also shown.

(Korde 2015). The intermediate-depth propagation model approximation-related errors are seen to have a strong frequency dependence at low frequencies, as expected (Figs. 5, 6). The one-parameter approximation is currently only designed for a particular dominant frequency. At high frequencies, where the parameter value A estimated for a low frequency is used, the error asymptotes to a small steady value depending on the difference $|g - A|$. The single-parameter approximation is moderately satisfactory over a small-frequency range, but at low frequencies as the propagation process approaches shallow-water non-dispersive propagation, the approximation diverges rapidly as would occur if a deep-water dispersion relation was to be applied in shallow water (the single parameter in that case, being g). It is important to point out that the treatment of Sect. 5.1 assumes that the various Bridgeprobe wave gauges are precisely phase-synchronized.

The time-series results of Fig. 7 predict the wave elevations $t_p = 9.53$ s into the future, at a propagation distance $x_p = 101$ m, which is the distance between two of the wave gages used in the tests. These results are obtained with the approximate propagation model. The wave input consisted of uni-directional irregular waves derived from wave spectra chosen as indicated in Sect. 6. For the beach layout, and the wave propagation direction (effective beach length increasing thanks to the action of beaches on two sides of the corner), reflections from the tank walls and the fixed model were estimated using measurements from a series of regular-wave test runs with the model held fixed. Figure 4 shows reflections over the frequency range 0.25–0.7 Hz. Based on this plot, reflections around 5% may be expected at 0.4 Hz, while close to 16% reflections could occur at frequencies in the range 0.6–0.7 Hz. It is likely that a considerable portion of the $\sim$ 15% at the higher frequencies is contributed by the model itself. The dominant frequency in the sea states used here for the wave prediction is close to the low-reflection ($\sim$ 5 %) range. However, the test wave fields include the higher frequencies where reflections may be greater. For this reason, it is expected that the conclusions based on these test results are subject to errors due to reflections. It should be noted that, because the beach reflections are frequency-dependent, the tank hydrodynamics with beach reflections may impose an additional transfer function on all tank measurements. This effect is not captured in the propagation model-based prediction, nor in the prediction based on Fourier coefficients. In addition, other sources of uncertainty in the experimental results, such as wave probe calibration relations and dynamic response, may be worth considering.

The wave elevation time-series results for three test runs with predictions based on the approximate propagation model show noticeable instantaneous excursion errors but relatively smaller lead/lag errors. The results plotted in Fig. 8 compare the measured time-series with predictions based on the technique using Fourier coefficients. These comparisons show noticeably greater differences in instantaneous excursions with greater lead/lag errors. It is likely that the prediction time and propagation distance are too large for some of the measurement points for the Fourier-coefficient-based approach, and a choice of measurement and prediction locations based on the space–time diagram would be worth considering for this approach (see also Sect. 8.2). In addition, it is worth noting that discretization-related errors are smaller for predictions based on the approximate propagation model, since the impulse-response function is obtained analytically. However, in this case, as suggested by Figs. 5 and 6, both errors (instantaneous wave excursions and lead/lag) are likely to be greater for longer periods.

As discussed earlier, the ability to use multiple-point wave elevation measurements brings forth the following advantage: point measurements at the distance d_p required by the prediction time t_p with the approximate propagation model approach: at longer prediction times and correspondingly longer measurement (and prediction) distances, error accumulation due to propagation model approximation may be significant. Combining results for longer distances with the more accurate results based on point measurements at shorter distances for shorter prediction times provides a corrective effect for the longer prediction times. If device dynamics require long prediction times and the device is to operate in intermediate water depths, the multiple-point measurement approach may lead to improved accuracy with analytically integrable approximate propagation models.

For the Fourier coefficient-based approach, error due to frequency discretization (i.e., discretization at a particular point may miss some frequencies with non-negligible wave input contribution) is mitigated by the use of multiple spatially distributed measurement points.

Figure 9 plots the time-series comparisons for the approximate propagation model with measurements at five points. Because of the mitigating effect of combining the predicted time-series for the different locations, the measured and predicted time-series appear to agree well on lead/lag (especially, peak/trough times) though less on instantaneous wave excursions.

It is instructive to compare the spectral composition of the predicted results with the measured-wave elevations, to form an idea of the frequency range where good agreement

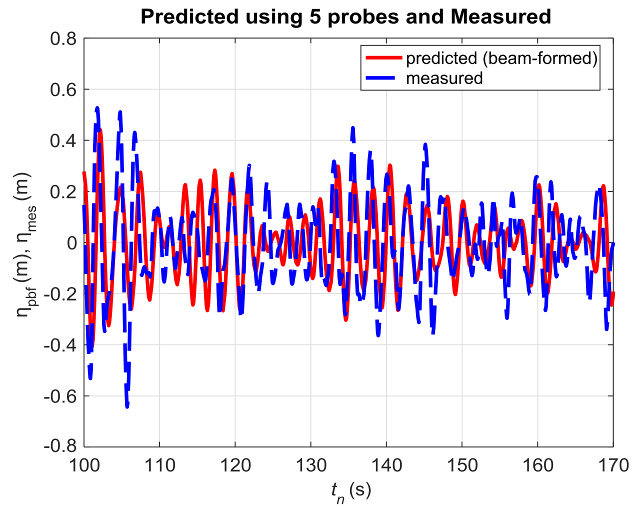

Fig. 9 Predicted vs. measured-wave elevations (proposed approximation with technique to combine multiple measurements): wave elevation time-series as predicted using the approximate intermediate-depth propagation model, when time-series at five points within the space–time diagram of Fig. 1 are combined. Experimental measurements for the prediction location are also shown.

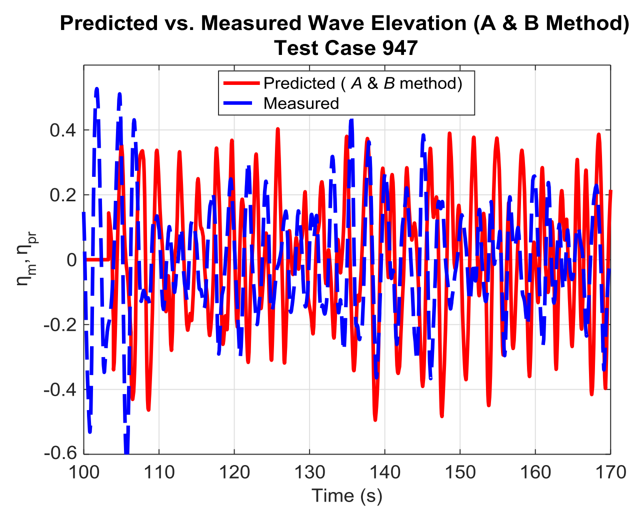

Fig. 10 Predicted vs. measured-wave elevations (Fourier coefficients using multiple measurements): wave elevation time-series as predicted using the method based on Fourier coefficients (A and B), by combining predictions based on the A and B coefficients at five points. Experimental measurements for the prediction location are also shown.

is not observed, which would shed light on the frequency range where the dispersion relation approximation is less effective for the propagation model-based technique. For the Fourier coefficient-based technique, the full dispersion relation is used to relate ω and k, but the frequency discretization implicit to the method is a possible source of error. Spectral amplitudes could provide an idea of what type of errors is dominant for each technique.

The Fourier spectra of Figs. 11 and 12 for the approximate propagation model show overview-level agreement between

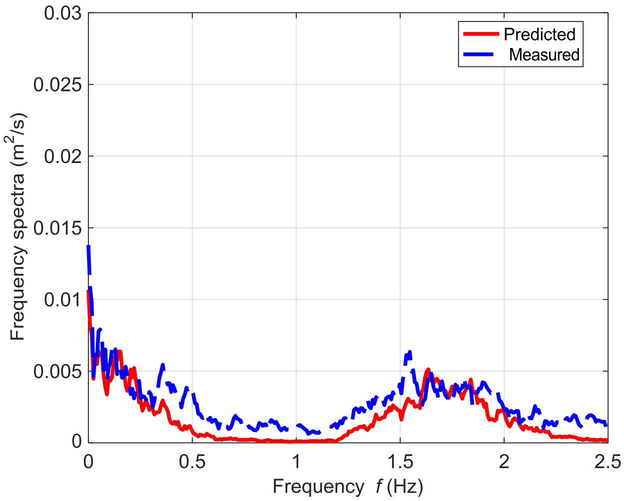

Fig. 11 Comparisons in frequency domain: Fourier transforms of the squared instantaneous wave elevations as predicted using the approximate intermediate-depth propagation model, when time-series at five points within the space–time diagram of Fig. 1 are combined. Fourier transforms of the squares of the experimental wave elevation measurements for the prediction location are also shown.

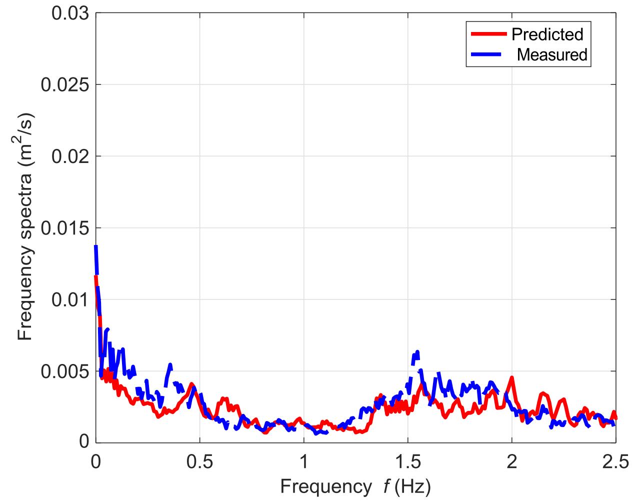

Fig. 12 Comparisons in frequency domain: Fourier transforms of the squared wave elevation time-series as predicted using the method based on Fourier coefficients (A and B) when predictions based on the A and B coefficients at five points are combined. Fourier transforms of the squares of the experimental measurements for the prediction location are also shown.

the predicted and measured-wave spectra. The measured-wave spectrum shows considerably greater frequency-domain oscillations, which could be a result of successive discretization (i.e., discretization for wave generation followed by sampling for wave measurement, followed by discretization for Fourier transformation). On the other hand, the propagation model-based prediction has a low-pass filter effect, given that the propagation distance and prediction time are based on a band-limited space–time diagram (in that some high-frequency slow-moving components may not yet have arrived at the measurement location). As Fig. 12 suggests, for the Fourier coefficient-based method, the band-limiting effect is absent not only for the measured-wave time-series but also for the Fourier coefficient fitting and prediction parts of the process in this case. For this reason, both spectra (measured and predicted) show considerable high-frequency content. Figure 13 compares the spectral contents in the prediction using the approximate analytical technique of Fig. 11 with the technique based on the A and B coefficients from Fig. 12.

The direct comparison of the two prediction approaches shows considerable disagreement over the entire frequency range, but in particular, in the mid-frequency range from 0.5 to 1.2 Hz. It appears the approximate analytical technique (with results over five points combined) is better optimized for the lower and higher frequencies, while the A and B method (with results over five points combined) seems better optimized for the middle-frequency range. It is likely that this difference may be due to the fact that contemporaneous measurements at multiple points were used to estimate A and B coefficients that were later utilized to obtain a prediction

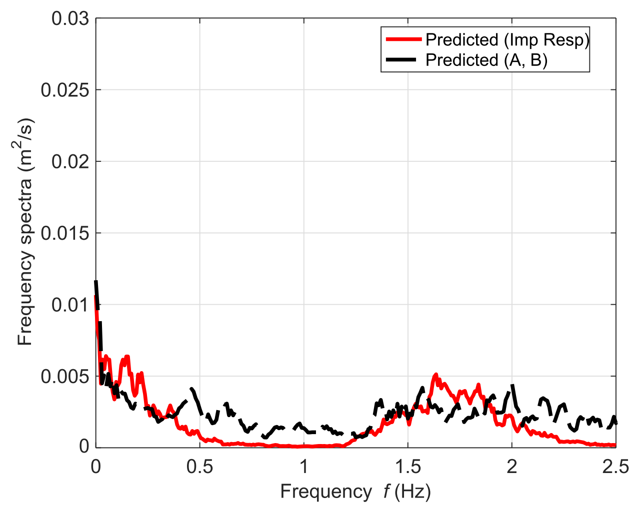

Fig. 13 Comparison of two approaches in frequency domain: Fourier transforms of squared instantaneous wave elevation time-series as predicted using **a** the approximate intermediate-depth propagation model with five point measurements, and **b** using the A and B coefficients for five points.

at a time a few seconds into the future. It should be noted that this is not the case with the way the five time-series are combined for the approximate propagation model-based approach (where the lengths and times of measurement were chosen based on the space-time diagrams). Wave excursion match is marginal for both approaches, and the reason for this mismatch needs to be studied further, as pointed out below, with some attention to any errors due to the presence of reflected waves in the tank measurements. Among the possible sources of error are as follows:

1. Model error: Both approximate intermediate-depth propagation model (despite being helped by the consolidation of five point measurements) and the spectral coefficient (A and B) model insufficiently capture the propagation process in the tank. For the small amplitudes used here, non-linear wave–wave interactions and other non-linear effects are likely very small, however.
2. Measurement error: The wave probe signals and the signal conditioning hardware may have introduced errors of phase and amplitude. In particular, if the wave probes are not precisely phase-synchronized, considerable phase errors may build up for longer probe separations.
3. Reflections: The reflection quantification study of Sect. 7 suggests the presence of frequency-dependent reflections from 5 to 12% of the incident-wave amplitudes. These could result in amplitude errors that are different for different frequencies in the sea state. Given the dispersion relation, these amplitude errors can lead to considerable phase errors as propagation distances increase.

Of the three sources listed above, the last seems the most likely dominant source of error. A possible improvement in future work may be to apply the technique in Sect. 7 over the entire distance range covered by the wave gauges used. This could be done using adjacent pairs of wave gauges to compute the incident-wave components in the space between each probe. Such an enhancement will help to account for tank attenuation effects, as well as for any phase errors due to imprecise phase synchronization between probes. It is expected that using the separated out incident-wave components to form the incident-wave elevation time-series will enable a true comparison of the two prediction techniques and the true effectiveness in intermediate water depths of the approximate propagation model with five-point consolidation approach. It is expected that the results of such an extension will enable a more reliable application of the approach for wave energy conversion in intermediate depths and for other marine applications in such depths.

For constrained impedance-matching control, however, it is more important to capture the temporal structure correctly, so that the actuator force can be controlled, such that it follows the correct lead/lag relationship with respect to the exciting-force temporal variation. For a single-mode device, or for devices whose response can be reduced to that of an equivalent single-mode response, velocity should be synchronous with the exciting force for best power conversion under displacement/velocity constraints. Since oscillation constraints are frequently needed for most devices, it is suggested that the impact of the wave excursion mismatch noted in this work could in practice be less limiting (than in the case of unconstrained oscillations).

Finally, it should be noted that there are intrinsic limits to how well wave-prediction tests in a wave tank represent testing in the real-sea environment. (i) the possible presence of tank-wall reflections may only be considered realistic for representing near-shore coastal regions; and (ii) the way irregular waves are frequently generated in wave tanks automatically results in a 'repeat period', which would produce a long-period signature in the wave elevation measurements. This effect does not occur in real-sea environments.

11 Conclusions

In this work, the focus was on obtaining deterministic wave elevation predictions in intermediate water depths. To that end, this work investigated an approach based on a convenient approximation that allowed an analytically derived approximate propagation impulse-response function. A straightforward convolution evaluation based on this impulse-response function provided the approximate prediction for the wave elevation at the device at the time instant required by the device dynamics. Given this approximation, the particular question addressed here was whether combining the predictions based on time-series measurements at multiple locations would improve the overall accuracy of the prediction at the device at the required time instant. For the propagation model-based approach, the manner in which predictions from multiple points are combined represents a rudimentary form of the beam-forming technique used in the case of electromagnetic and acoustic waves (Kumatani et al. 2012), and an analogous matched-field processing approach discussed in Baggeroer et al. (1993) for acoustic wave propagation in the ocean.

For comparison, an alternative technique based on Fourier coefficients (estimated at each measurement point) was also used. Experimental measurements made in the U.S. Navy MASK basin in Carderock, MD were utilized in this study. Uni-directional irregular-wave records at multiple points along the propagation direction were available. Measurements at five points along the propagation direction were chosen based on their locations relative to the model to be tested. Wave predictions were obtained at a sixth up-wave point representing the location where the model would be located. The predicted time-series were compared with the measured time-series. Time-domain comparisons showed plausible agreement for the approximate propagation model (in terms of the individual peaks and troughs being synchronous), though instantaneous wave excursion agreement was modest. For the prediction distance and prediction time used here, combining the predictions based on measurements at five locations enhanced lead/log accuracy, which may be considered more important for wave-by-wave impedance-matching control of wave energy devices under displacement and force constraints (Korde 2019). Results based on Fourier coefficients could be improved by determining the time-series lengths and prediction times based on a space–time diagram.

Future work should consider a more detailed accounting of reflections as experienced at each wave gauge location. Further work should include multi-directional waves with a predominant direction, modeled after commonly encountered directional sea states at chosen intermediate-depth locations as well as suitably planned at-sea testing. Applications outside of wave energy conversion such as real-time ship-motion prediction for ship-board and other operations may also be worth investigating.

Acknowledgements UAK is grateful to the Sandia National Laboratories for supporting this work. All three authors wish to thank the U.S. Department of Energy Water Power Program for their support. Sandia National Laboratories is a multi-mission laboratory managed and operated by National Technology and Engineering Solutions of Sandia, LLC., a wholly owned subsidiary of Honeywell International, Inc., for the U.S. Department of Energy's National Nuclear Security Administration under contract DE-NA0003525. This paper describes objective technical results and analysis. Any subjective views or opinions that might be expressed in the paper do not necessarily represent the views of the U.S. Department of Energy or the United States Government.

References

Al-Ani M, Christmas J, Belmont MR (2019) Deterministic sea-waves prediction using mixed space-time radar wave data. J Atmos Ocean Technol 36:834–841

Baggeroer AB, Kuperman WA, Mikhalevsky PN (1993) An overview of matched field methods. IEEE J Ocean Eng 18(4):401–424

Belmont MR, Horwood JMK, Thurley RWF, Baker J (2006) Filters for linear sea-wave prediction. Ocean Eng 33(17–18):2332–2351

Belmont MR, Horwood JMK, Thurley RWF, Baker J (2007) Shallow angle wave profiling lidar. J Atmos Ocean Technol 24(6):1150–1156

Belmont MR, Christmas J, Dannenberg J, Hilmer T, Duncan J, Duncan JM, Ferrier B (2014) An examination of the feasibility of linear deterministic sea wave prediction in multidirectional seas using wave profiling radar: Theory, simulation, and sea trials. J Atmos Ocean Technol 31:1601–1614

Brownell W (1962) Two new hydromechanics research facilities at the David Taylor Model Basin. Tech. rep., Department of the Navy: David Taylor Model Basin, Technical Report 1690

Budal K, Falnes J (1977) Optimum operation of improved wave power converter. Mar Sci Commun 3:133–150

Coe R, Bacelli G, Spencer S, Cho H (2018) Initial results from wave tank tests of close-loop WEC control. Tech. rep., Sandia National Laboratories, SAND2018-12858

Cretel JAM, Lightbody G, Thomas GP, Lewis AW (2011) Maximization of energy capture by a wave-energy point absorber using Model Predictive Control. In: Proc. 18th IFAC world congress, September 2011, Milano, Italy

Dannenberg J, Naaijen P, Hessner K, den Boom H, Reichert K (2010) The on board wave and motion estimator OWME. In: Proc. int. soc. offshore and polar engr. Conf., Beijing, China

Evans DV (1976) A theory for wave power absorption by oscillating bodies. J Fluid Mech 77(1):1–25

Evans DV (1981) Power from water waves. Annu Rev Fluid Mech 13:157–187

Falnes J (1995) On non-causal impulse response functions related to propagating water waves. Appl Ocean Res 17(6):379–389

Garcia-Abril M, Paparella F, Ringwood JV (2017) Excitation force estimation and forecasting for wave energy applications. IFAC-PapersOnline 50(1):14692–14697

Goda Y, Suzuki Y (1976) Estimation of incident and reflected waves in random wave experiments. In: 15th coastal engineering conference, pp 828–845

Gran S (1987) Lectures in ocean engineering-waves and wave forces. Tech. rep., University of Oslo and A/S Veritas, Norway

Korde UA (2015) Near-optimal control of a wave energy device using deterministic-model driven incident wave prediction. Appl Ocean Res 53:31–45

Korde UA (2019) Wave energy conversion under constrained wave-by-wave impedance matching with amplitude and phase-match limits. Appl Ocean Res 90:101858

Korde UA, Richon JB (2018) Recent experimental testing of a 2-body wave energy converter under wave-by-wave impedance matching control. Technical report to the National Science Foundation, U.S

Korde UA, Ringwood JV (2016) Hydrodynamic control of wave energy devices. Cambridge University Press, Cambridge

Korde UA, Robinett RD, Wilson DG, Bacelli G, Abdelkhalik OO (2017) Wave-by-wave control of a wave energy converter with deterministic wave prediction. In: Proc. 12th European wave and tidal energy conference (EWTEC), Cork

Korde UA, Coe RG, Bacelli G (2019) Deterministic wave elevation prediction for wave-by-wave impedance matching of wave energy devices. In: Proc. water power week—marine technology symposium, Washington, D.C.

Kumatani K, McDonough J, Raj B (2012) Microphone array processing for distant speech recognition. IEEE Signal Process Mag 29:127–140

Liao Z, Stansby P, Li G (2020) A generic linear non-causal optimal control framework integrated with wave excitation force prediction for multi-mode wave energy converters with application to m4. Appl Ocean Res 97:102056

Maa J (2013) Coherence length of realistic wave fields. Virginia Institute of Maritime Sciences. William and Mary College **(personal communication)**

Mansard E, Funke E (1980) Measurement of incident and reflected spectra using a least-squares method. In: 17th intl. conference on coastal engineering, Sydney, pp 95–96

Naito S, Nakamura S (1985) Wave energy absorption in irregular waves by feedforward control system. In: Evans D, de O Falcão A (eds) Proc. IUTAM symp. hydrodynamics of wave energy utilization. Springer, Berlin, pp 269–280

Newman JN (1978) Marine hydrodynamics, second Printing, Call No. (VM 156.N48). MIT Press, Cambridge, pp ix + 402

Newman JN (1979) Absorption of wave energy by elongated bodies. Appl Ocean Res 1(4):189–196

Press WH, Teukolsky HA, Vetterling W, Flannery BP (1986) Numerical recipes: the art of scientific computing, 1st edn. Cambridge University Press, Cambridge

Qi Y, Wu G, Liu Y, Kim M, Yue D (2018) Nonlinear phase-resolved reconstruction of irregular water waves. J Fluid Mech 838:544–572

Salter SH (1974) Wave power. Nature 249:720–724